Nature Communications

https://doi.org/10.1038/s41467-026-69681-w

Article in Press

Sub-5 nm high-entropy nanoalloys beyond the hume-rothery limit

Received: 31 July 2025

Accepted: 6 February 2026

Cite this article as: Du, Y., Zhou, X., Li, B. *et al.* Sub-5 nm high-entropy nanoalloys beyond the hume-rothery limit. *Nat Commun* (2026). https://doi.org/10.1038/s41467-026-69681-w

Yiqian Du, Xiaodi Zhou, Bangxin Li, Zhizhong Wang, Enyuan Zhou, Yihao Liu, Huibin Zhang, Xuhui Xiong, Jiacheng Cui, Hualiang Lv & Renchao Che

Sub-5 nm High-Entropy Nanoalloys Beyond the Hume-Rothery Limit

Yiqian Du, Xiaodi Zhou, Bangxin Li, Zhizhong Wang, Enyuan Zhou, Yihao Liu, Huibin Zhang, Xuhui Xiong, Jiacheng Cui, Hualiang Lv*, Renchao Che*

Laboratory of Advanced Materials, Institute of Optoelectronics, College of smart materials and future energy, Fudan University, Shanghai 200438, P. R. China.

*Corresponding author.

Yiqian Du 22113010024@m.fudan.edu.cn

Xiaodi Zhou 23113010024@m.fudan.edu.cn

Bangxin Li bxli22@m.fudan.edu.cn

Zhizhong Wang 24210300072@m.fudan.edu.cn

Enyuan Zhou 24210300116@m.fudan.edu.cn

Yihao Liu yihao_liu@fudan.edu.cn

Huibin Zhang zhb18814726293@163.com

Xuhui Xiong 22113010020@m.fudan.edu.cn

Jiacheng Cui jccui23@m.fudan.edu.cn

Hualiang Lv* lv_hl@fudan.edu.cn

Renchao Che* rcche@fudan.edu.cn

Abstract

Lattice mismatch has long constrained alloy compositional design. Governed by the Hume-Rothery rules, severe atomic radius differences (δ) between the constituent elements of nano-alloys can lead to excessive lattice distortions or even phase separation. Therefore, synthesizing alloy nanoparticles with large δ-factors (>15%) is almost impossible, restricting structural and functional tunability. Here, we report a general plasma-assisted carbothermal flash sintering (PCFS) synthesis strategy to obtain sub-5 nm high-entropy alloys (HEAs) nanoparticles with δ-factors exceeding 15%. Plasma treatment helps compensate for the entropy reduction caused by high-δ, while non-equilibrium ultrafast synthesis prevents slow nucleation under thermodynamic steady-state conditions. Utilizing high-entropy to introduce medium-sized bridging elements, large atoms (lanthanides, >180 pm) and small atoms (Al) are successfully accommodated in a single-phase nanolattice with ordered lattice distortions. The resulting quasi-periodic lattice distortions (QPLD) formed via stress relief minimize structural defects and enable anomalous electronic and thermal transport properties. These nanoscale HEAs achieve an exceptional electromagnetic interference (EMI) shielding efficiency of ~99% at a thickness of only ~1.8 μm, which is two orders of magnitude thinner than conventional materials. This general strategy unlocks thousands of possible element combinations, providing a broad materials platform for advanced electronics, energy, and device applications.

Introduction

Expanding the compositional space of nano-alloys, particularly multi-component alloys with severe atomic radius mismatches, remains a fundamental challenge[1]. Central to this difficulty is the tension between lattice tolerance and thermodynamic stability. The Hume–Rothery (H–R) rules[2,3] has long served as a guiding guideline for predicting solid-solution formation, stating that excessive differences in atomic radii and composition destabilize the alloy and favor phase separation. The radius difference is usually quantified by δ[4]:

$$\delta\% = \sqrt{\sum_{i=1}^{n} c_i \left(1 - \frac{r_i}{\bar{r}}\right)^2} \times 100\% \quad (1)$$

where c_i represents the atomic fraction of element i in the alloys, and r denotes its atomic radius. At the nanoscale, the H-R rules become more stringent due to lattice strain, surface effects, and kinetic barriers[5]. Considering the high specific surface area and limited configurational freedom, even moderate atomic size mismatches can lead to severe structural disruption manifested by increased atomic defects, reduced coordination number, weakened metallic bonds, and uneven stress distribution[6].

High-entropy alloys[7] (HEAs) have attracted widespread interest by breaking through the phase separation that was induced by component complexity. The random distribution of multiple principal elements within the crystal lattice displaces constituent atoms from their ideal positions, giving rise to pronounced lattice distortion[8,9]. Such distortion has been recognized as a key contributor to the thermodynamic nonequilibrium state of HEAs[10] and is closely associated with their distinctive properties[11-13]. Recent empirical research has illuminated that the lattice distortion inherent in HEAs exhibits a pronounced dependency on particle size[14]. As the dimensions of HEAs shrink to the nanoscale, the lattice distortion is markedly intensified due to the increasingly irregular interactions among the constituent atoms[15]. Enhanced distortion drives an increase in system entropy[16], promoting atomic rearrangement and facilitating the formation of high-δ HEAs nanoparticles (NPs). These insights suggest that compositionally rich HEA-NPs with severe atomic radius mismatches are feasible and possess broad potential for applications in efficient catalysis, clean energy conversion, and electronic devices.

However, various methods employed for synthesizing HEA-NPs, such as wet chemical[17-19], annealing[20-22], dropwise[23], and rapid Joule heating[24,25], remain constrained by the classical H-R rules. Even when configuration entropy[26] (ΔS_{conf}) and mixing enthalpy (ΔH^{SS}) appear favorable, large δ often lead to phase separation or amorphization. In fact, beyond ΔS_{conf}, the reduction in excess entropy[27,28] (ΔS_{ex}) associated with atomic size differences is central to determining phase

states. At the solubility limit, enthalpy cannot compensate for the required entropy reduction, leading to phase separation.

Inspired by the electronic metal support interaction (EMSI) introduced by Campbell[29] *et al.*, we supposed that interface-induced charge transfer could be exploited to stabilize high-δ HEA-NPs. Here, we propose a universal plasma-assisted carbon thermal flash sintering (PCFS) strategy that effectively addresses the above challenges and accesses thousands of possible composition combinations. Sub-5 nm HEA-NPs with δ-factors exceeding 15% were prepared by plasma-assisted, ultrafast, and nonequilibrium synthesis. Large-size atoms (lanthanides, > 180 pm) and small-size atoms (e.g., Al, ~118 pm) are successfully accommodated in a single-phase nanolattice by bridging elements of intermediate atomic radius. We observe that the combination of severe atomic radius differences and ultrasmall HEAs induces profound atomic reconstruction, leading to quasi-periodic lattice distortions (QPLD) with minimal defects and anomalous electronic properties. Notably, these properties offset the conductivity loss typically observed in nanometals and surpass that of most known conductors of comparable size. Furthermore, the anomalous electronic transport enables HEA-NPs to achieve ~99% electromagnetic interference (EMI) shielding efficiency at a thickness of ~1.8 μm, nearly two orders of magnitude thinner than conventional materials, highlighting its great potential for micron-scale EMI shielding encapsulation materials.

Result

A general strategy for synthesizing few-nanometer HEAs with severe atomic radius differences

The relationship between δ and particle size (d) in recently reported HEA-NPs is shown in **Fig. 1a** and **Supplementary Tables S1-2**. A clear trend emerges as particle size decreases to the few-nanometer scale, δ typically falls below 15%. To elucidate this trend, we applied machine learning[30] (ML) models to analyze the underlying interdependencies, as detailed in **Supplementary Note 1** and **Fig. S1**. δ in HEAs influences factors such as mixing enthalpy (ΔH_{mix}), conformational entropy (ΔS_{conf}), electronegativity ($\Delta\chi$), and valence electron concentration (VEC). Size variations, in turn, affect the specific surface area (S_{sp}), surface atomic energy (γ), and other properties. As shown in **Fig. 1b**, these factors are interdependent and directly impact the stability and the formation of HEAs, as demonstrated by the significant SHapley Additive exPlanations[31] (SHAP) values. To probe this effect on entropy more deeply, **Fig. 1c** illustrates the correlation between δ and system entropy (ΔS). Initially, the entropy in high-entropy alloys is primarily dominated by ΔS_{conf}, with the ΔS_{ex} arising from atomic size differences being negligible (**Supplementary Note 2**). However, as δ exceeds the threshold defined by the H-R rules, excessive

size mismatch destabilizes the system, rendering ΔS_{ex} no longer ignorable. In such instances, larger atoms may aggregate and undergo recrystallization, whereas smaller atoms tend to cluster separately, fostering phase separation or the emergence of indeterminate phases such as amorphous states[32], polycrystalline structures, or intermetallic[33]. Significant differences in the *VEC*, $\Delta\chi$, and orbital energies of different metals lead to these phenomena, thus complicating the formation of stable metallic bonds. The observations are supported by the bonding capacity between atoms calculated using the Crystal Orbital Hamilton Populations[34] (COHP) theory. (**Fig. 1d** and **Supplementary Note 3**). Such atomic segregation ultimately reduces overall disorder, diminishing the high-entropy stabilization effect. Furthermore, as *d* decreases, quantum size effects become increasingly significant, modifying the distribution and localization of electron orbitals (**Fig. 1e**). These effects induce orbital displacement and distortion, reduce effective orbital overlaps, and further hinder the formation of robust metallic bonds across diverse atomic environments.

To synthesize few-nanometer HEA-NPs characterized by significant atomic radius differences, we developed a plasma-assisted carbon flash sintering (PCFS) method. Plasma-induced modulation of surface and interfacial work functions was synergistically combined with rapid heating-cooling cycles to synthesize nanoscale high-δ HEAs. As shown in the schematic (**Supplementary Fig. S2**) and the HADDF-STEM images (**Supplementary Fig. S3**), our methodology encompasses three primary stages: (i) carbon substrate chemical treatment and metal salt adsorption; (ii) a first heating-cooling cycle to control the nucleation and growth of metallic NPs on carbon substrates, ensuring uniform size and structural stability (**Supplementary Fig. S4**) and (iii) plasma treatment to modify the substrate's work function (**Supplementary Fig. S5**), followed by a second cycle to facilitate uniform atomic reconfiguration (**Supplementary Fig. S6**). Plasma irradiation lowers the surface work function of the carbon nanotubes[35], facilitating electron transfer from carbon to HEA-NPs. We suggest that nanoparticles increase the delocalized electron density[36], exhibiting enhanced metallic bonding that contributes to enthalpy reduction[37]. Meanwhile, electron enrichment elevates the density of states near the Fermi level (E_f), increasing electron entropy[38,39] (ΔS_{elec}). Notably, nanosizing also facilitates surface entropy[40,41] (ΔS_{surf}) to compensate for ΔS, further stabilizing high-δ alloy structures (**Supplementary note 2**). Subsequent CFS steps provide high-energy excitation, inducing atoms to overcome diffusion barriers and rearrange, tending to form a single-phase solid solution. Furthermore, from a kinetic perspective, the HEA-NPs prepared via PCFS are kinetically trapped (metastable). PCFS-derived nanoparticles undergo ultrafast heating-cooling cycles at the nanoscale diffusion length, effectively freezing the distorted solid solution before long-range distribution occurs. Our technique permits the synthesis of HEAs with the potential to encompass most metallic elements

from the periodic table[42], excluding Li and radioactive metals, thereby exhibiting exceptional compositional versatility and tunability (**Fig. 2a** and **Supplementary Figs. S7-15**). Furthermore, this method also enables precise control over particle size, crystal structure (e.g. metal heterostructures, amorphous structures, clusters, or single atoms), atomic ratios, and δ of HEAs. The products can be tuned by manipulating the carbon substrate work function and sintering temperature during the PCFS process, as guided by the relevant phase diagrams[43] (**Fig. 2b** and **Supplementary Figs. S16-19**).

Leveraging this multidimensional tunability, we have designed a series of sub-5 nm HEAs based on FeCoNi as the primary *bcc* phase, supplemented by lighter elements Al and elements from the lanthanide series, thereby ensuring a pronounced radius difference. For instance, the representative FeCoNiAlPr HEAs demonstrates that the NPs display a consistent size distribution of approximately 4.8 ± 1.9 nm, are monodisperse on the carbon substrate, and exhibit a homogeneous elemental distribution of Fe, Co, Ni, Al, and Pr, as evidenced by the low-resolution high-angle annular dark-field scanning transmission electron microscopy (HAADF-STEM) image shown in **Fig. 2c**. The elemental compositions of Fe, Co, Ni, Al, and Pr were precisely quantified using inductively coupled plasma optical emission spectroscopy (ICP-OES), revealing mass ratios of 28.92 ± 0.6 wt%, 23.23 ± 0.7 wt%, 20.84 ± 0.3 wt%, 9.55 ± 0.4 wt%, and 17.46 ± 0.2 wt%, respectively. These values are consistent with the elemental contents statistically determined from multi-particle STEM-EDS mapping (**Supplementary Fig. S20**). The detailed X-ray photoelectron spectroscopy (XPS) spectra and fitting results of FeCoNiAlPr HEA-NPs (**Supplementary Fig. S21** and **Table S3**) reveal that all five elements exhibit metallic behavior[44]. The Al^{3+} and Pr^{3+} peaks arise from incomplete reduction during synthesis and are attributed to trace residual metal salts. Weak characteristic metal peaks in the X-ray diffraction (XRD) spectrum confirm the ultrafine size of the nanoparticles (**Supplementary Fig. S22**). It is shown that the lattice is dominated by Fe-*bcc* as the main phase, with Fe, Co and Ni as major elements, and Al and Pr acting as minor substituting elements in the lattice. The FeCoNiAlPr HEA-NPs exhibit a remarkable δ of 18.14 %, which represents an increase of approximately 70-80% over those reported in current studies, while maintaining an average size of only 4.8 nm.

To further explore the elemental distribution and its impact on the lattice structure, aberration-corrected scanning transmission electron microscopy (AC-STEM) was employed to obtain electron energy loss spectroscopy (EELS) and atomic-resolution HAADF-STEM images. To eliminate artifacts caused by scanning coil misalignment and image drift, these images undergo further refinement through phase difference calculations[45] and calibration enhancement techniques[46]. EELS scans were performed along the indicated trajectories (lines 1-3) of

FeCoNiAlPr NPs (**Fig. 2d**). Analyses performed at a scan width of 1.0 nm showed that line scan trace contained Fe, Co, Ni, Al and Pr. Atomic-resolution STEM-EDS mapping analysis also demonstrates uniform distribution of elements within individual nanoparticles (**Supplementary Fig. S23**). It has been demonstrated that the elements are randomly distributed in the NPs without any preferred orientation. For comparison, representative FeCoNiCuZn (δ=3.5%), FeCoNi (δ=1.5%), and Fe NPs with a uniform size of ~4.0 nm was synthesized using a similar approach (**Supplementary Fig. S24**). **Fig. 2e** demonstrates the atomic structure of the core and edge of FeCoNiAlPr HEA-NPs. The atomic arrangement shows obvious ordered distortions, and the edge lattice is regular and organized. The distortions originate from the lattice misalignment of stress release upon δ increase, indicating that the synthesized NPs exhibit QPLD, as shown by geometrical phase analysis (GPA) (**Fig. 2f**). In contrast, the comparison samples exhibit irregular local lattice distortions and prominent surface defects, leading to reduced coordination numbers and disordered stress distributions (**Supplementary Fig. S25**). Additionally, the lattice of FeCoNiAlPr shows no obvious defects such as vacancies or layer faults although it exhibits obvious periodic distortions extending from the surface to the interior. It is confirmed by the Extended X-ray Absorption Fine Structure (EXAFS) analysis of Fe. The κ-space amplitude of FeCoNiAlPr closely resembles that of pure Fe foil, in sharp contrast to FeCoNiCuZn, which displays a significantly attenuated amplitude—indicative of a reduced average coordination number[48] (**Fig. 2g** and **Supplementary Fig. S26**). It is consistent with the results of the R-space least-squares fit, further confirming the absence of significant structural defects in the FeCoNiAlPr sample that would reduce the coordination number **(Supplementary Table S4**).

Analysis of Conductivity and Thermal Transport Characteristics

Conventional nanometal surfaces have a disordered atomic arrangement due to quantum size effects. Such structural alterations modify the electron wavefunctions, induce the formation of discrete energy levels[49], and severely compromise or even eradicate the electronic transport properties of metallic NPs[50]. The emergence of high-entropy, driven by potential atomic rearrangement and the cocktail effect, helps alleviate this constraint[51]. Illustratively, we investigate the size-dependent electrical conductivity (σ) of various Fe-based metals, focusing on the FeCo alloy, the FeCoNi medium-entropy alloy (MEA), and the FeCoNiCuZn HEAs. As depicted in **Fig. 3a**, a notable increase in the electrical conductivity of the FeCoNiCuZn alloy is observed as the particle size diminishes from 10^6 nm to 1 nm.

Furthermore, the QPLD phenomenon observed in high-δ HEAs mitigates lattice defects, thereby reducing electron scattering. We evaluated the electrical transport properties of

FeCoNiAlPr HEA-NPs using the Hall effect. The FeCoNiAlPr film demonstrated a carrier concentration (n_e) ranging from 6.08×10^{20} to 6.83×10^{20} cm^{-3} and mobility (μ_H) between 49.5 and 57.8 $cm^2V^{-1}s^{-1}$ within the 300-600 K temperature range. These values are improved by 11-57% and 229-920%, respectively, compared to FeCoNiCuZn HEA-NPs and other low- and medium-entropy conducting metals of comparable size, as presented in **Fig. 3b** and **Supplementary Fig. S27**. The FeCoNiAlPr conductivity was elevated to between 6000 and 7000 S/cm, which is double the conductivity observed in FeCoNiCuZn (**Supplementary Fig. S28d**). Meanwhile, size-dependent analyses in the bulk-nanoscale range show that the electrical conductivity of FeCoNiAlPr is 1-5 times higher than that of current HEAs, conducting polymers, and 2D materials. Remarkably, this performance is on par with that of bulk conductive metals such as Ag and Au, as well as advanced carbon materials including MXene, graphene, and carbon nanotubes, as shown in **Fig. 3c** and **Supplementary Table S5**.

To gain deeper insight into the underlying mechanism, density functional theory (DFT) calculations were performed. Conventional HEAs (3%-10%) exhibit a random atomic distribution that varies with $\Delta\chi$, leading to local potential fluctuations and lattice distortions. Such structural perturbations result in enhanced band dispersion, disrupted band symmetry, and an expanded distribution of electronic states[52]. It was confirmed by comparative analysis of representative systems involving the elements Fe, FeCoNi, and FeCoNiCuZn, as depicted in **Supplementary Fig. S28**. Conversely, a significant decrease in band dispersion is observed for FeCoNiAlPr alloys exhibiting larger δ. The resulting band flattening helps to minimize the effect of external random potential on the electrons in the lattice. Consequently, electronic states accumulate rapidly near the Fermi level, significantly elevating the density of states[53], as illustrated in **Fig. 3d** and **Supplementary Fig. S29**.

Here, we need to clarify that this enhancement typically occurs in HEAs with sufficiently large δ. The highly heterogeneous local chemical environment at each lattice site leads to pronounced atomic displacements and dramatic fluctuations in local potentials. The regular overlap of atomic orbitals is disrupted, thus reducing electron hopping between neighboring atoms. Such phenomena are corroborated by charge distribution analyses (**Supplementary Fig. S30**). Despite the presence of local perturbations, the potential tends to return to neutrality at the macroscopic scale due to the inherent stochastic nature of the elemental distribution within the HEAs. The restoration of uniformity is substantiated by measurements of local charge differences. As a result, the electronic structure becomes symmetric, encouraging the development of flat, nearly degenerate energy bands at points of high symmetry within the Brillouin zone. The density of states near the Fermi level is greatly increased, facilitating a multi-channel synergistic electron transport mechanism.

Beyond a sufficiently large δ, reducing the size of HEAs to the nanoscale plays a critical role in enhancing their properties. To demonstrate this effect, we introduced a PLD of approximately 6% into the unit cell in our computational model, which closely corresponds to the experimentally observed QPLD at the nanoscale. As shown in **Supplementary Fig. S31**, the band further flattens as the lattice distortion is enhanced[54]. The minimal energy separation among these nearly degenerate states facilitates the effect of even minor external perturbations, thereby promoting efficient mixing and transitions between states. As a result, the FeCoNiAlPr alloy, characterized by its pronounced atomic radius mismatch, demonstrates notably enhanced electrical conductivities. Furthermore, the enhancement is closely related to alloy nanosizing. The high surface energy at the nanoscale promotes the reconstruction of surface atoms, and the internal stress relaxation mitigates the local strain, further stabilizing the lattice structure.

In addition, the FeCoNiAlPr film exhibited a thermal conductivity (κ_T) of approximately 38.2-30.1 W/m·K across the 300-600 K temperature range, representing an improvement of about four times compared to the same-sized FeCoNiCuZn alloys. Notably, this corresponds to 55-45% of the thermal conductivity typical of bulk metals (~70 W/m·K), as shown in **Fig. 3e**. It is also demonstrated by DFT calculations concerning phonons, as shown in **Fig. 3f** and **Supplementary Fig. S32**. The enhancement of the group velocity of FeCoNiAlPr in the vicinity of low frequencies favors the suppression of phonon scattering. Stability assessments (**Supplementary Fig. S33**) confirm that 4.8nm FeCoNiAlPr NPs maintain stable crystal structures even after prolonged atmospheric exposure, as verified by high-resolution HADDF-STEM. Structural reliability ensures thermal and electrical transport properties, highlighting their potential for high-temperature electronics and advanced thermal management applications. In summary, our investigations underscore that the strategic design of nanoscale HEAs, leveraging significant atomic radius disparities, can effectively counteract the quantum effects that typically impair the performance of nanometals. The electrical, thermal, and chemical properties realized in this way are comparable to, and in some cases even exceed those of bulk metals.

Extended application of HEAs-filled shielding layer in advanced packages

The dense stacking of electronic components is a promising strategy for achieving high-performance, miniaturized electronics that support more complex computations and enhanced functionality[55]. However, advances in integration have also increased the power density. The enhanced current and high-frequency switching lead to higher heat and electromagnetic radiation, as shown in **Fig. 4a**. Consequently, signal interference and heat accumulation become significant impediments to the performance, lifespan, and reliability of integrated electronics. Given that these

components typically operate at the micron or nanometer scale, there is an urgent need to develop solutions that provide superior electromagnetic shielding and effective heat dissipation layers. Traditional materials, such as conductive polymers (e.g., epoxy resin, silicone), semiconductor materials (e.g., silicon carbide, ceramics), and bulk metals (e.g., Cu, Ag, Al), face challenges in meeting these dual demands while also supporting the trend toward miniaturization[56]. Therefore, a single-layer, micro/nanoscale packaging solution that optimally provides both shielding and heat dissipation remains a highly desirable yet challenging goal.

To address this need, we believe that the nanometer-sized HEAs we have developed offer a compelling solution[57]. As shown in **Fig. 4b**, incorporating merely 10 wt% of 4.8 nm-FeCoNiAlPr into silicone results in an average shielding effectiveness of 99.9% at a 1.8 μm thickness across the 2-6 GHz frequency range used by current fifth generation (5G) wireless networks. The exceptional electromagnetic shielding performance is attributable to the alloy's ultrahigh permittivity, driven by its high electrical conductivity. Detailed investigations of the corresponding shielding coeffcient and percolation threshold are presented in **Supplementary Figs. S34** and **S35**, along with **Note 4**. In contrast, traditional electromagnetic materials such as MXenes, graphene, and CNTs typically require thicknesses that are one to three orders of magnitude greater to achieve similar levels of shielding effectiveness, as shown in **Fig. 4c** and **Supplementary Table S6**. Meanwhile, the shielding film demonstrates excellent stability across the temperature range of 300-600 K, ensuring reliability for electronic components exposed to temperature fluctuations, as demonstrated in **Fig. 4d**, **Supplementary Fig. S36**, and **Note 5**. Beyond shielding, we also observed that its thermal conductivity reaches 5.8 W/m·K even at this ultralow filling ratio, significantly surpassing the performance of polymer-based heat dissipation layers, as indicated in **Supplementary Table S7**. In summary, we have developed nanoscale HEAs with excellent electromagnetic shielding, efficient heat dissipation, and support for miniaturization, providing a solution for shielding layers in advanced packages.

To further demonstrate its practical application, we observed that our developed nanoscale HEAs (δ > 15%) are suitable for electronic components of various sizes, as shown in the digital images in **Fig. 4e**. Moreover, with the Graphics Processing Unit (GPU) running at full load for 20 mins, the temperature of the shielding layer is only 16.9 K higher than the ambient temperature, which stays at 273 K. Under similar conditions, the temperature rise of conventional HEAs is 53.3 K. As shown in **Fig. 4f**, the comparison highlights the superior thermal management performance of our developed HEAs.

Discussion

In summary, we report a novel synthesis method for high-entropy alloy nanoparticles (HEA-NPs), achieving the first preparation of nano-HEAs that break the conventional Hume–Rothery rules. The plasma-assisted carbothermal flash sintering (PCFS) enabled the realization of HEA-NPs with unprecedented atomic radius differences (δ > 15%) and sub-5 nm sizes. The PCFS process further affords broad structural and compositional tunability: metallic glasses, intermetallic compounds, and HEA-NPs containing thousands of components can all be synthesized within a unified framework. Specifically, entropy compensation strategies and non-equilibrium dynamics were key factors. The formation of high-δ solid solutions is supported by direct structural evidence. Atomic-resolution imaging reveals a quasi-periodic lattice distortion (QPLD) that accommodates the large size mismatch while preserving single-phase character. These nanoparticles remain in a kinetically trapped state, exhibiting high crystallinity, minimal defect density, and coherent lattice distortion rather than the random distortion common in bulk HEAs. Notably, the conductivity of these HEAs outperform state-of-the-art nanomaterials of comparable size (e.g., graphene, MXene), achieving ~99% electromagnetic shielding efficiency at a thickness of only ~1.8 μm, which is two orders of magnitude thinner than conventional materials. Future work will customize the HEA atomic configuration to enable new physical phenomena and multifunctional applications.

Methods

Synthesis of high-entropy alloy precursors

All the HEA-NPs reported in this paper were loaded on a carbonized polyacrylonitrile (PAN) substrate. The PAN was dissolved in dimethylformamide (DMF) and then electrostatically spun at a voltage of 15 kV, a spinning distance of 15 cm, and a feed rate of 4 mL/h. The spinning collector roller spun at 100 rpm. The precursors were subsequently carbonized at 500 K in an air environment for 2 h and subsequently stabilized at 1100 K in an argon environment for 1 h. Prior to impregnation with salt solution, the precursors were sintered in a carbon dioxide environment at 1000 K for 3 h to better adsorb the carbon nanotubes to the salt solution. In the case of FeCoNiAlPr, for example, the carbonized PAN was impregnated with a mixed chloride salt solution at a concentration of 0.05 mol/L for 2 h, then centrifuged and dried to obtain the precursor.

Synthesis of FeCoNiAlPr HEA-NPs.

The HEA-NPs underwent the CFS process twice. The impregnated carbon nanofiber powder was placed on carbon paper, with graphite plates clamped at both ends for rapid Joule heating. The entire chamber underwent three cycles of argon gas purging, maintaining a negative pressure of approximately 0.05 MPa. After ultra-rapid heating, the temperature naturally cooled to room temperature. The sintering temperature and time were adjusted to realize the regulation of the components and particle size. Taking FeCoNiAlPr HEA-NPs as an example, 100 mg of the impregnated precursor was taken for the first sintering at 2000 K for 0.2 s, and then processed by a plasma cleaner with a power of 300 W under vacuum for 20 s. The final sintering process was carried out after 1500 K for 0.5 s for the second sintering, uniform FeCoNiAlPr NPs with a diameter of about 3-5 nm were obtained.

Structural characterization

The morphology, atomic structure, and elemental distribution of the HEAs were characterized using field-emission transmission electron microscopy (FETEM, JEOL JEM-2100F, 200 kV) and aberration-corrected transmission electron microscopy (AC-TEM, FEI Spectra 300, 300 kV). EELS data were collected using a Gatan imaging filter detector with an energy resolution of 0.5 eV at zero-loss peaks and an energy dispersion of 0.2 eV per channel. The crystal structure was analyzed using X-ray diffraction (XRD, Bruker D8 Advance) with Cu Kα radiation ($\lambda = 0.15406$ nm). The chemical composition was determined using X-ray photoelectron spectroscopy (XPS, Thermo Scientific Nexsa G2). X-ray absorption spectroscopy (XAS) measurements were performed at beamline BL14W1 of the Shanghai Synchrotron Radiation Facility (SSRF). The X-ray absorption near-edge structure (XANES) and extended X-ray absorption fine structure (EXAFS) spectra were analyzed using the Athena and Artemis software packages. The elemental

composition of the HEAs was accurately quantified using inductively coupled plasma optical emission spectrometry (ICP-OES) spectroscopy.

Characterization of electrical, thermal, and electromagnetic properties

The electrical carrier mobility and carrier concentration were measured using a Hall effect measurement system (Ecopia HMS-7000). The 10 × 10 mm square wafers (thickness < 0.3 mm) were mounted in a four-probe fixture and measured under a 100 mA constant current. Hall voltage and resistivity were recorded from 300 to 600 K at 25 K intervals. The thermal conductivity was measured using a thermal constants analyzer (Hot Disk TPS 2500S) following the ISO 22007-2:2015 standard. Disk-shaped pellets (~10 mm diameter, ~1 mm thickness) were prepared by cold pressing the alloy powders at 10 MPa. The testing was conducted at a temperature of 20 °C, and each sample was measured once. To ensure the reliability of the results, at least three independent samples were tested for each group, and the averaged values were used as the experimental data. The EM and S-parameters used to evaluate the electromagnetic shielding were obtained from a vector network analyzer (Keysight, N5234A).

DFT details

Density functional theory (DFT) calculations were performed using the Vienna Ab initio Simulation Package (VASP 5.4.4). Exchange-correlation effects were treated within the generalized gradient approximation (GGA) using the Perdew-Burke-Ernzerhof (PBE) functional. The projector-augmented wave (PAW) method was employed, with pseudopotentials from the VASP PBE 5.4 library. For Pr, we employed the pseudopotential Pr_3, wherein the 4f electrons are treated as part of the frozen core. This is because the 4f states of Pr exhibit high localization and do not participate in metallic bonding. Furthermore, since the 4f electrons are excluded from the valence space, DFT+U corrections are neither applied nor required. The other elements (Fe, Co, Ni, Al, Cu and Zn) used standard PBE pseudopotentials. The plane-wave kinetic energy cutoff was set to 520 eV, and the k-point spacing of 0.04 $Å^{-1}$ was used to sample the Brillouin zone. The total energies were converged to 10^{-5} eV, and atomic positions were relaxed until residual forces were below 0.01 eV $Å^{-1}$. All models were treated with P1 symmetry to account for the inherent asymmetry of HEAs. For HEAs structures, special quasi-random structures (SQS) were generated by simulating random atomic arrangements using Python code. The main SQS supercell contained 54 atoms (3×3×3 expansion). The atom coordinates of the structurally optimized model are provided in the supporting file.

Phonon dispersion and group velocities were computed using the finite displacement method. Due to the stringent accuracy requirements of phonon calculations, the supercell structures were optimized with tighter convergence criteria of 10^{-10} eV for energy and 10^{-7} eV/Å for forces. Post-

processing of electronic and phonon properties was carried out using the VASPKIT 1.5.1 and Phonopy 2.38 software packages.

Chemical bonding analysis was performed using LOBSTER 5.1.1 to obtain crystal orbital Hamilton population (COHP) curves. The plane wave is projected onto local atomic orbitals using the PBE pseudopotential basis set in self-consistent calculations, and the total charge spilling was kept below 1 %, confirming the accuracy of the projection. Integrated COHP (−ICOHP) values were used to quantify metallic bond strengths.

Data availability

Source Data are provided with this paper. Relevant data supporting the key findings of this study are available within the article and the Supplementary Information file.

References

1 Liu, J. & Zhang, J. Nanointerface Chemistry: Lattice-Mismatch-Directed Synthesis and Application of Hybrid Nanocrystals. *Chem. Rev.* **120**, 2123-2170 (2020).

2 Mizutani, U., Sato, H. & Massalski, T. B. The original concepts of the Hume-Rothery rule extended to alloys and compounds whose bonding is metallic, ionic, or covalent, or a changing mixture of these. *Prog. Mater Sci.* **120**, 100719 (2021).

3 Hume-Rothery, W. & Powell, H. M. On the Theory of Super-Lattice Structures in Alloys. *Zeitschrift für Kristallographie-Crystalline Materials* **91**, 23-47 (1935).

4 Miracle, D. B. & Senkov, O. N. A critical review of high entropy alloys and related concepts. *Acta. Mater.* **122**, 448-511 (2017).

5 Takrori, F. M. & Ayyad, A. Surface energy of metal alloy nanoparticles. *Appl. Surf. Sci.* **401**, 65-68 (2017).

6 Halperin, W. P. Quantum size effects in metal particles. *Rev. Mod. Phys.* **58**, 533-606 (1986).

7 George, E. P., Raabe, D. & Ritchie, R. O. High-entropy alloys. *Nat. Rev. Mater.* **4**, 515-534 (2019).

8 Yeh, J.-W. Physical Metallurgy of High-Entropy Alloys. *JOM* **67**, 2254-2261 (2015).

9 Wang, H. *et al.* Multifunctional High Entropy Alloys Enabled by Severe Lattice Distortion. *Adv. Mater.* **36**, 2305453 (2024).

10 Zeng, Y. *et al.* High-entropy mechanism to boost ionic conductivity. *Science* **378**, 1320-1324 (2022).

11 He, Q. F. *et al.* A highly distorted ultraelastic chemically complex Elinvar alloy. *Nature* **602**, 251-257 (2022).

12 Lee, C. *et al.* Strength can be controlled by edge dislocations in refractory high-entropy alloys. *Nat. Commun.* **12**, 5474 (2021).

13 Jiang, B. *et al.* High-entropy-stabilized chalcogenides with high thermoelectric performance. *Science* **371**, 830-834 (2021).

14 Wang, B. *et al.* General synthesis of high-entropy alloy and ceramic nanoparticles in nanoseconds. *Nat. Synth.* **1**, 138-146 (2022).

15 Cao, G. *et al.* Liquid metal for high-entropy alloy nanoparticles synthesis. *Nature* **619**, 73-77 (2023).

16 Yao, Y. *et al.* Computationally aided, entropy-driven synthesis of highly efficient and durable multi-elemental alloy catalysts. *Sci Adv* **6**, eaaz0510 (2020).

17 Minamihara, H. *et al.* Continuous-Flow Reactor Synthesis for Homogeneous 1 nm-Sized Extremely Small High-Entropy Alloy Nanoparticles. *Journal of the American Chemical Society* **144**, 11525-11529 (2022).

18 Ai, Y. *et al.* Ultra-Small High-Entropy Alloy Nanoparticles: Efficient Nanozyme for

Enhancing Tumor Photothermal Therapy. *Adv. Mater.* **35**, 2302335 (2023).

19 Wang, Y. *et al.* Unconventional Interconnected High-Entropy Alloy Nanodendrites for Remarkably Efficient C−C Bond Cleavage toward Complete Ethanol Oxidation. *Angew. Chem. Int. Ed.* **64**, e202420752 (2025).

20 Li, H. *et al.* Fast site-to-site electron transfer of high-entropy alloy nanocatalyst driving redox electrocatalysis. *Nat. Commun.* **11**, 5437 (2020).

21 Mori, K. *et al.* Hydrogen spillover-driven synthesis of high-entropy alloy nanoparticles as a robust catalyst for CO2 hydrogenation. *Nat. Commun.* **12**, 3884 (2021).

22 Hao, J. *et al.* Unraveling the electronegativity-dominated intermediate adsorption on high-entropy alloy electrocatalysts. *Nat. Commun.* **13**, 2662 (2022).

23 Liu, Y.-H. *et al.* Toward controllable and predictable synthesis of high-entropy alloy nanocrystals. *Science Advances* **9**, eadf9931 (2023).

24 Yao, Y. *et al.* Carbothermal shock synthesis of high-entropy-alloy nanoparticles. *Science* **359**, 1489-1494 (2018).

25 Yao, Y. *et al.* Extreme mixing in nanoscale transition metal alloys. *Matter* **4**, 2340-2353 (2021).

26 Yeh, J.-W. *et al.* Nanostructured High-Entropy Alloys with Multiple Principal Elements: Novel Alloy Design Concepts and Outcomes. *Adv. Eng. Mater.* **6**, 299-303 (2004).

27 Mansoori, G. A., Carnahan, N. F., Starling, K. E. & Leland, T. W., Jr. Equilibrium Thermodynamic Properties of the Mixture of Hard Spheres. *The Journal of Chemical Physics* **54**, 1523-1525 (1971).

28 Ye, Y. F., Wang, Q., Lu, J., Liu, C. T. & Yang, Y. High-entropy alloy: challenges and prospects. *Mater. Today* **19**, 349-362 (2016).

29 Campbell, C. T. Electronic perturbations. *Nat. Chem.* **4**, 597-598 (2012).

30 Liu, X., Zhang, J. & Pei, Z. Machine learning for high-entropy alloys: Progress, challenges and opportunities. *Prog. Mater Sci.* **131**, 101018 (2023).

31 Lundberg, S. M. & Lee, S. I. in *31st Annual Conference on Neural Information Processing Systems (NIPS).* (2017).

32 Wang, H. *et al.* Deformation-induced crystalline-to-amorphous phase transformation in a CrMnFeCoNi high-entropy alloy. *Sci. Adv.* **7**, eabe3105 (2021).

33 Cui, M. *et al.* Multi-principal elemental intermetallic nanoparticles synthesized via a disorder-to-order transition. *Sci. Adv.* **8**, eabm4322 (2022).

34 Zhou, J. *et al.* Boridene: Two-dimensional $Mo_{4/3}B_{2-x}$ with ordered metal vacancies obtained by chemical exfoliation. *Science* **373**, 801-805 (2021).

35 Dey, A., Chroneos, A., Braithwaite, N. S. J., Gandhiraman, R. P. & Krishnamurthy, S.

Plasma engineering of graphene. *Applied Physics Reviews* **3** (2016).

36 Pacchioni, G. & Freund, H.-J. Controlling the charge state of supported nanoparticles in catalysis: lessons from model systems. *Chem. Soc. Rev.* **47**, 8474-8502 (2018).

37 Ubaru, S., Międlar, A., Saad, Y. & Chelikowsky, J. R. Formation enthalpies for transition metal alloys using machine learning. *Phys. Rev. B* **95**, 214102 (2017).

38 Widom, M. Modeling the structure and thermodynamics of high-entropy alloys. *J. Mater. Res.* **33**, 2881-2898 (2018).

39 Widom, M. & Gao, M. First Principles Calculation of the Entropy of Liquid Aluminum. *Entropy* **21**, 131 (2019).

40 Tyson, W. R. & Miller, W. A. Surface free energies of solid metals: Estimation from liquid surface tension measurements. *Surface Science* **62**, 267-276 (1977).

41 Molleman, B. & Hiemstra, T. Size and shape dependency of the surface energy of metallic nanoparticles: unifying the atomic and thermodynamic approaches. *Physical Chemistry Chemical Physics* **20**, 20575-20587 (2018).

42 Pauling, L. Atomic Radii and Interatomic Distances in Metals. *Journal of the American Chemical Society* **69**, 542-553 (1947).

43 Yao, Y. et al. Carbothermal shock synthesis of high-entropy-alloy nanoparticles. *Science* 359, 1489-1494 (2018).

44 Powell, C. J. Recommended Auger parameters for 42 elemental solids. *J. Electron. Spectrosc. Relat. Phenom.* **185**, 1-3 (2012).

45 Jones, L. & Nellist, P. D. Identifying and Correcting Scan Noise and Drift in the Scanning Transmission Electron Microscope. *Microscopy and Microanalysis* **19**, 1050-1060 (2013).

46 Oni, A. A. *et al.* Large area strain analysis using scanning transmission electron microscopy across multiple images. *Appl. Phys. Lett.* **106** (2015).

47 Subhash, B. et al. Resolving Atomic-Scale Structure and Chemical Coordination in High-Entropy Alloy Electrocatalysts for Structure-Function Relationship Elucidation. *ACS Nano* 17, 22299-22312 (2023).

48 Wang, Y. *et al.* Layered Double Hydroxide Nanosheets with Multiple Vacancies Obtained by Dry Exfoliation as Highly Efficient Oxygen Evolution Electrocatalysts. *Angew. Chem. Int. Ed.* **56**, 5867-5871 (2017).

49 Paggel, J. J., Miller, T. & Chiang, T. Quantum-well states as fabry-Perot modes in a thin-film electron interferometer. *Science* 283, 1709-1711 (1999).

50 Volokitin, Y. et al. Quantum-size effects in the thermodynamic properties of metallic nanoparticles. *Nature* 384, 621-623 (1996).

51 Ching, W.-Y. *et al.* Fundamental electronic structure and multiatomic bonding in 13 biocompatible high-entropy alloys. *npj Comput. Mater.* **6**, 45 (2020).

52 Li, K. et al. High-Entropy Strategy to Achieve Electronic Band Convergence for High-Performance Thermoelectrics. *J. Am. Chem. Soc.* 146, 14318-14327 (2024).

53 Lv, H. et al. Functional nanoporous graphene superlattice. *Nat. Commun.* 15, 1295 (2024).

54 Zhao, P. et al. Ultrahigh Thermal Robustness of High-Entropy Spectrally Selective Absorbers for Next-Generation Concentrated Solar Power System. *Adv. Funct. Mater.* 34, 2411316 (2024).

55 Choi, C. et al. Reconfigurable heterogeneous integration using stackable chips with embedded artificial intelligence. *Nat. Electron.* 5, 386-393 (2022).

56 Li, R. et al. Review on polymer composites with high thermal conductivity and low dielectric properties for electronic packaging. *Mater. Today Phys.* 22, 100594 (2022).

57 Apell, P. & Ljungbert, Å. A General Non-Local Theory for the Electromagnetic Response of a Small Metl Particle. *Phys. Scr.* **26**, 113-118 (1982).

Acknowledgements

This work was supported by the National Natural Science Foundation of China (No. 12327804, 52231007, T2321003, 22088101, 22405050), the National Key Research Program of China (No. 2024YFA1208902, 2024YFA1408000, 2021YFA1200600), the Science and Technology Commission of Shanghai Municipality (No. 24ZR1406400), and Shanghai Municipal Education Commission (No. 24KXZNA06).

Author Contributions

Y.D., X.Z., B.L. contributed equally to this work. Y.D., X.Z., R.C., and H.L. conceptualized and designed experiments, directed research, and participated in manuscript writing. Y.D., X.Z., B.L., Z.W., E.Z., and H.Z. conducted material synthesis and performed various characterizations, involving SEM, TEM, XRD, XPS and XAFS. Y.D., Y.L., H.Z., and J.C. designed and conducted experiments on electricity, heat and electromagnetism. Y.D., H.Z., and X.X. carried out DFT simulations and machine learning model training. All authors contributed to data interpretation, discussions, and manuscript preparation.

Competing Interests

The authors declare that they have no competing interests.

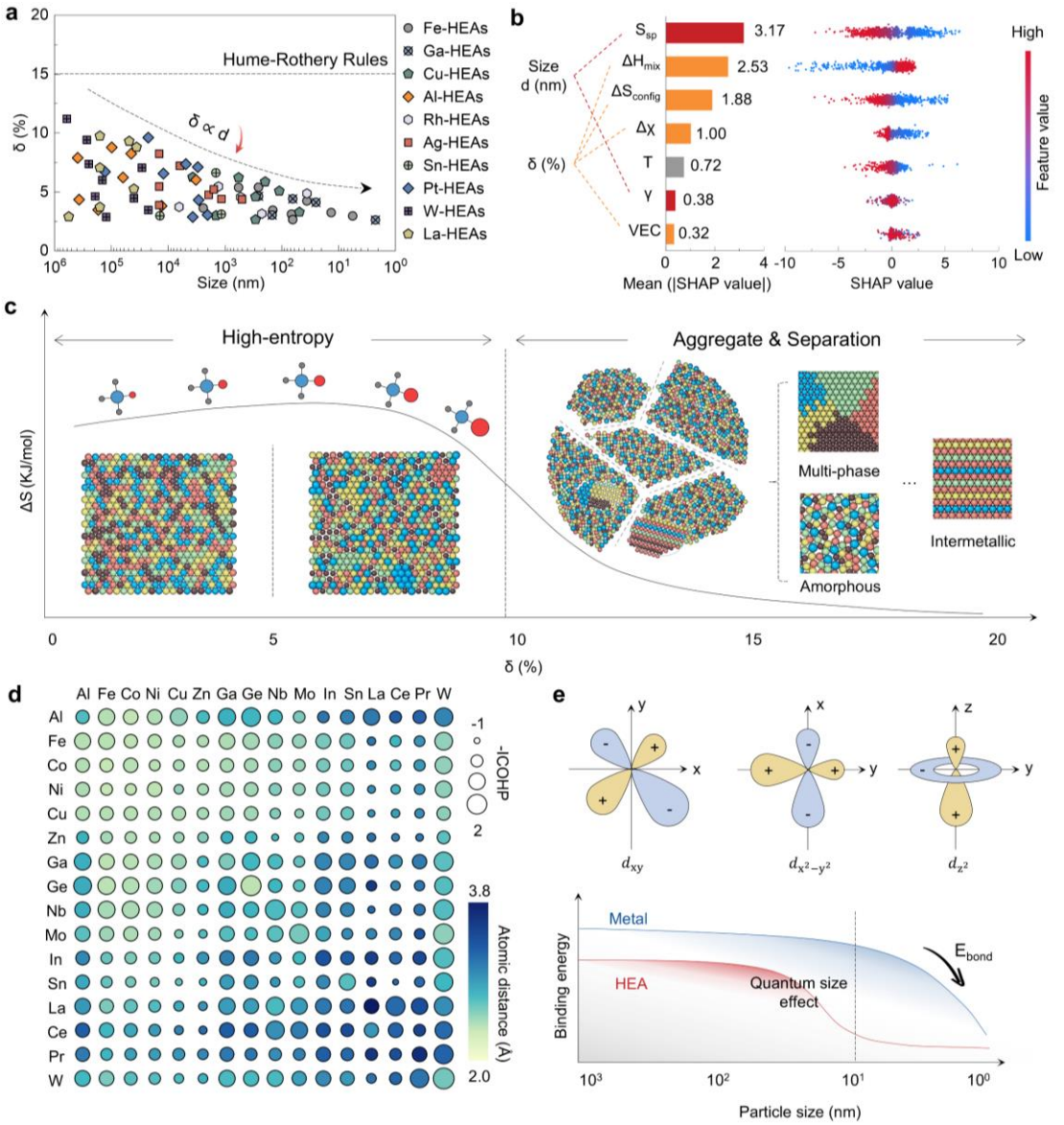

Fig. 1. Influencing factors on the Formation of Nanoscale HEAs. (a) Statistical plots of HEAs at the micrometer to nanometer scale versus δ-factor. Detailed data is provided in Supplementary Table 1. **(b)** The average SHAP histograms of the influencing factors and the swarm plots representing the eigenvalues and SHAP values of the predicted instances. Among the influencing factors are specific surface area (S_{sp}), conformational entropy (ΔS_{conf}), mixing enthalpy (ΔH_{mix}), electronegativity difference ($\Delta\chi$), synthesis temperature (T), surface energy (γ), and valence electron concentration (VEC). See Supplementary Note 1 for details. **(c)** Schematic diagram of structural evolution and system entropy (ΔS) of HEAs with increasing δ factor. Different colors represent distinct single metallic atomic species. **(d)** COHP calculations for bonding between different metals. **(e)** Schematic of orbital distortions due to quantum size effects and curves of the metal binding energy as a function of size nanosizing.

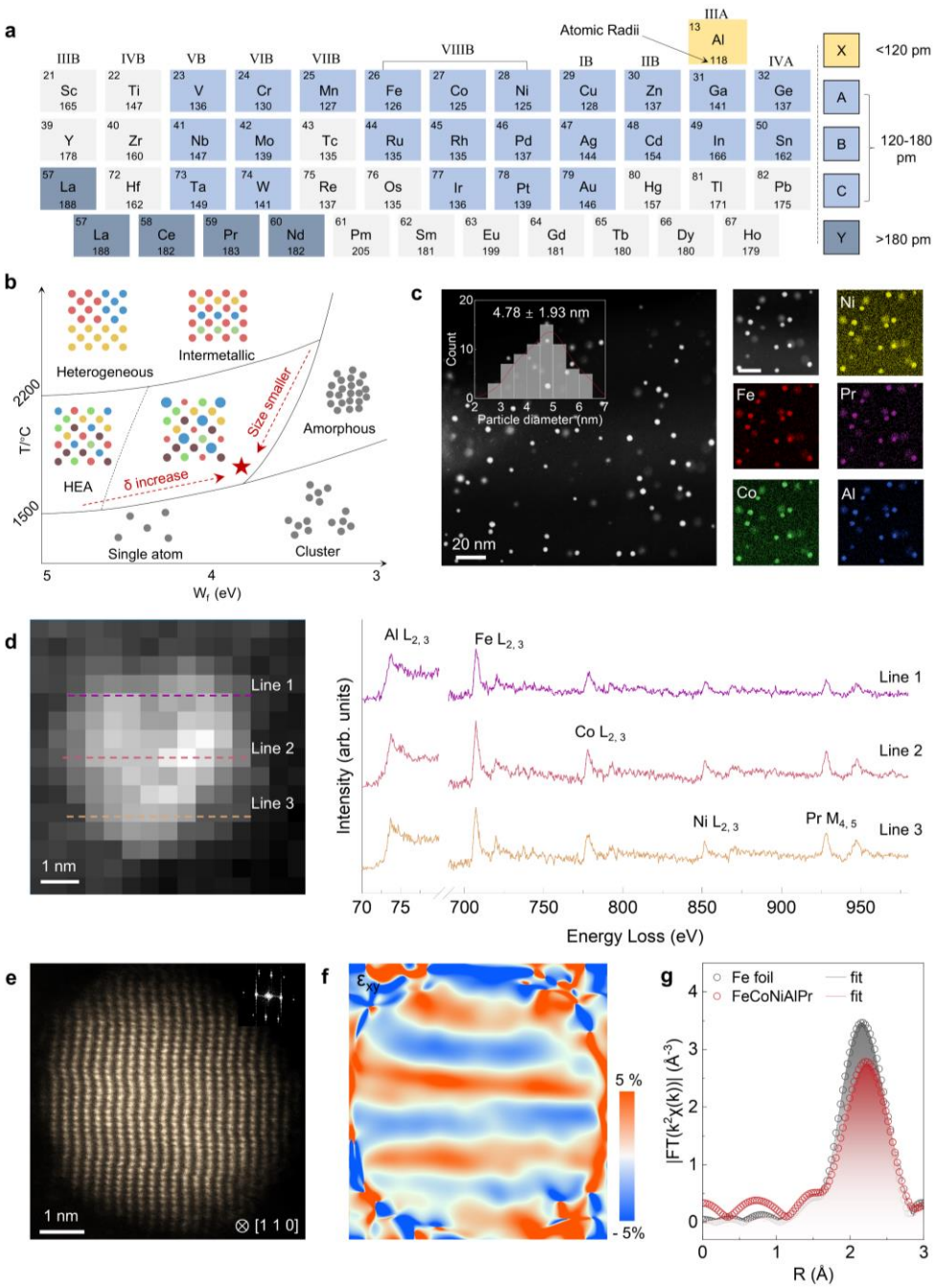

Fig. 2. General synthesis, generalization and microscopic characterization of HEA-NPs. (a) Periodic Table of Elements for Synthesizing Large *δ*-Factors HEA-NPs. **(b)** Phase diagram of FeCoNiAlPr NPs. The control variables are the work function of the substrate and the synthesis temperature. Gray denotes a high-entropy mixture of elements, while all other colors represent distinct single metallic atomic species. **(c)** Low magnification of HADDF-STEM and elemental mapping images. **(d)** ADF image and EELS spectra of FeCoNiAlPr NPs along line 1-3. **(e)** Atom-resolution HADDF-STEM image of FeCoNiAlPr NPs along [110] direction. **(f)** Geometric phase analysis (GPA) ε_{xy} strain map corresponding to Fig. 2e. **(g)**

EXAFS R-space spectra of FeCoNiAlPr NPs and Fe foil.

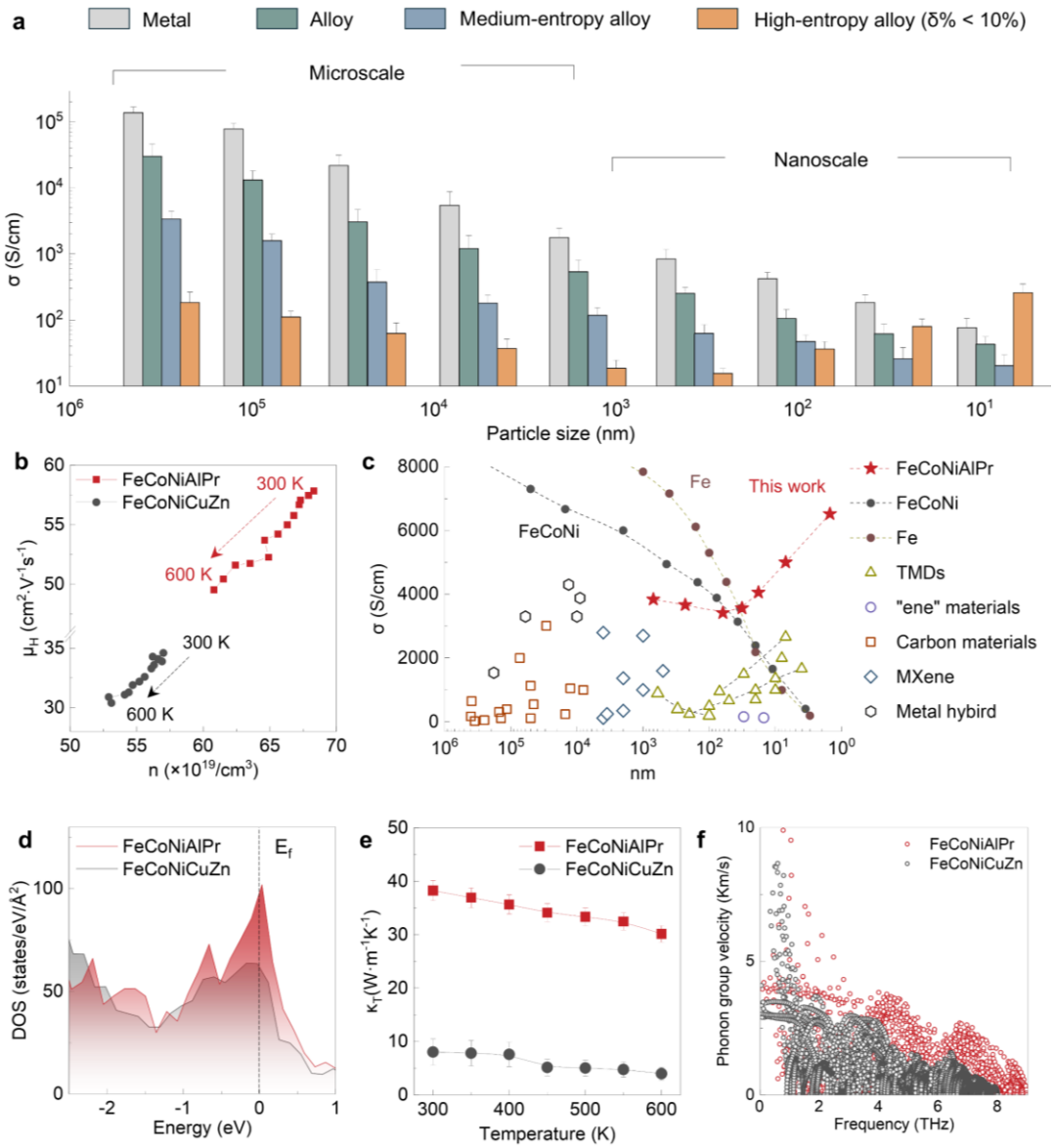

Fig. 3. Physical properties of FeCoNiAlPr HEA-NPs. (a) Variation of conductivity with size for metals and alloys with different values of entropy. Error bars represent the range, n=3. **(b)** Carrier mobility and concentration of HEA-NPs at 300-600K. **(c)** Comparison of conductivity with size variation has been reported for different materials. Detailed data is provided in Supplementary Table 5. **(d)** Density of states. **(e)** Thermal conductivity of 300-600K NPs. Error bars represent the range, n=3. **(f)** Phonon group velocity.

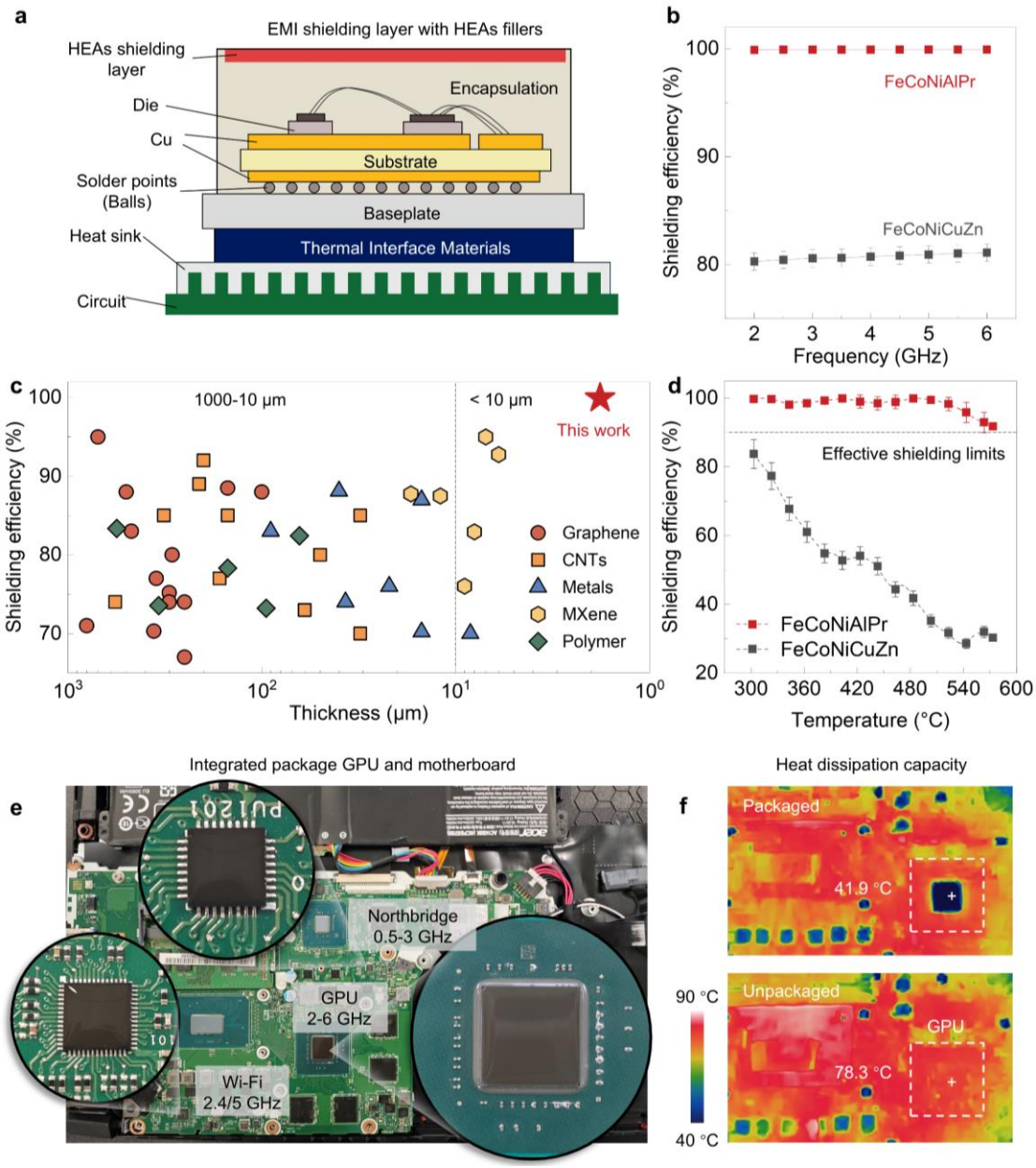

Fig. 4. Extended application of HEAs-filled shielding layer in advanced packages

(a) Schematic diagram of HEAs package. **(b)** Shielding efficiency of FeCoNiCuZn and FeCoNiAlPr films at 2-6 GHz. Error bars represent the range, n=3. **(c)** Comparison of shielding efficiency. Detailed data is provided in Supplementary Table 6. **(d)** Shielding efficiency of FeCoNiCuZn and FeCoNiAlPr NPs at 300-600℃. Error bars represent the range, n=3. **(e)** FeCoNiAlPr HEA-NPs coated on GPU and motherboard chips. **(f)** Infrared imaging comparison before and after coating of FeCoNiAlPr HEA-NPs.

Editor's Summary:

Atomic radius differences between the constituent elements of nano-alloys can lead to excessive lattice distortions or even phase separation. This work reports a plasma-assisted carbothermal flash sintering strategy for the synthesis of sub-5 nm high-entropy alloy nanoparticles accommodating large- and small-size atoms.

Peer review information: *Nature Communications* thanks Chanho Lee and the other, anonymous, reviewer(s) for their contribution to the peer review of this work. A peer review file is available.